

Cold Plasma Jet Coupled Nanosecond Laser Ablation Scheme For Plasmonic Nanostructured Surfaces

Taj Muhammad Khan,* Nazim Aslam, Amjad Iqbal, Shahab Ahmed Abbasi, and Dilawar Ali

This paper describes a study where an argon cold plasma jet, generated by a dielectric-barrier discharge (DBD), is combined with nanosecond laser ablation (248 nm, 25 ns, 10 Hz) to deposit silver particle aerosols onto the substrate at atmospheric pressure. The deposition of the particle is examined using various microscopy techniques and absorption spectroscopy for the plasma jet produced by operating DBD in the normal and reversed mode. Plasma facilitated the deposition process by delivering the particle to the substrate and significantly influenced its morphology depending on the jet interaction, length, and substrate position. In both cases, the particles are clustered; however, there is less deposit for the plasma ignited in the reverse mode. The theoretical analysis of the deposition process is performed using ANSYS software and evaluated in terms of plasma-induced flow velocity. This study infers that the hybrid plasma-laser deposition scheme considered is attractive for material processing and deposition, especially overextended substrate distances, and for altering the properties of the deposited particles for practical utilization in surface-enhanced Raman spectroscopy, solar cells, and catalysis.

such as sensors, subwavelength waveguides, photocatalysis, solar cells, enhanced fluorescence, and surface-enhanced Raman spectroscopy (SERS).^[1–3] Silver nanoparticles (NPs)-coated plasmonic active surfaces are offering optoelectronic, thermal, and biological properties.^[4] They are conductive (with the highest electrical conductivity of $6.3 \times 10^7 \text{ Sm}^{-1}$), transparent, less brittle, and chemically resistive—making them suitable candidates for high-performance and long-lasting flexible electrodes, touch screens of modern smartphones, flat panel televisions, and solar cell technologies.^[5–9]

The fabrication of plasmonic active nanomaterials and surfaces in industrially favorable atmospheric conditions can momentarily facilitate large-scale applications. Previously, chemical methods such as sol-gel, hydrothermal, spray pyrolysis, chemical bath

deposition, and physical methods including magnetron sputtering, atomic layer deposition, and pulsed deposition have been used to make these materials.^[9–17] Chemical methods use water

1. Introduction

Energy-harvesting plasmonic nanostructures of silver and gold have been extensively investigated for entrancing applications

T. M. Khan
National Institute of Lasers and Optronics College
Pakistan Institute of Engineering and Applied Sciences
Nilore, Islamabad 45650, Pakistan
E-mail: khanta@tcd.ie


T. M. Khan
School of Physics and CRANN
Trinity College Dublin
the University of Dublin
Dublin 2 Ireland

N. Aslam, S. A. Abbasi
Department of Physics
University of Azad Jammu and Kashmir
Muzaffarbad 13100, Pakistan

A. Iqbal
Department of Advanced Materials Technologies
Faculty of Materials Engineering
Silesian University of Technology
Gliwice 44-100, Poland

A. Iqbal
CEMMPRE - Centre for Mechanical Engineering
Materials and Processes
Department of Mechanical Engineering
University of Coimbra
Rua Luis Reis Santos, Coimbra3030-788, Portugal

D. Ali
Department of Physics
GC University
Lahore 54000, Pakistan

 The ORCID identification number(s) for the author(s) of this article can be found under <https://doi.org/10.1002/admi.202300280>

© 2023 The Authors. Advanced Materials Interfaces published by Wiley-VCH GmbH. This is an open access article under the terms of the Creative Commons Attribution License, which permits use, distribution and reproduction in any medium, provided the original work is properly cited.

DOI: 10.1002/admi.202300280

or organic solvents and employ three main components: metal precursors, reducing agents, and stabilizing/capping agents for the preparation of nanosilver. The process is done under specific conditions of temperature and pressure, usually in a heated reaction chamber under vacuum, and using a surfactant to manipulate the material properties. There is often a possibility of impurity traces that remain in the final product. Physical methods offer several advantages but require vacuum chambers and expensive vacuum pumps that make these methods more complex and have increased overall cost. Contrary to this, atmospheric pulsed laser deposition (APLD) has emerged as a simpler and more cost-effective method that does not require high-vacuum chambers and expensive vacuum pumps. Due to the feasible work environment, it is easy to deal with almost all types of substrates. Being an inexpensive and faster deposition method, it offers a viable platform to make various nanomaterials. Contrary to laser ablation in a vacuum, in the ambient condition, the interaction of the laser pulse of sufficient energy with a solid target ablates a thin surface layer and forms a nonexpanding plasma plume near the target surface. The ablation plume moves pretty slowly (500 ms^{-1} at $1.4 \text{ J} \cdot \text{cm}^{-2}$) due to the ambient constraints and its expansion is restricted to a couple of millimeters.^[1] In such a scenario, the deposition of the ablation material over a widely spaced substrate is a major concern to address. Coupling a plasma jet with the ablation process can assist the deposition process—the ablation material is entrained with the plasma outflow and can be delivered to the substrate for deposition.

Previously, pulsed laser deposition under vacuum has been widely investigated for particulate solid films of silver and gold for SERS and Ni NPs for catalysis applications.^[16–18] Nowadays, APLD has emerged as a scorching research topic in the frontier of nanofabrication. A preliminary investigation into APLD is looking at the viability of this method; (i) to confiscate the requirements of high-vacuum chambers and expensive vacuum pumps, (ii) to reduce the operation cost, and (iii) to provide a flexible and relatively faster nanofabrication platform to meet the today's requirement in nanotechnology. In the past two decades, tremendous efforts were devoted to the practical realization of APLD and a wide range of nanomaterials were produced.^[19–33] Although APLD has shown promise, there have been some issues that need to be addressed such as localized surface deposition, surface etching, and small target-to-substrate distance. Recent studies conducted by Khan et al. have demonstrated the viability of APLD with a vertically directed flowing gas jet of 32 ms^{-1} , which has effectively transported the particle aerosol onto the substrate.^[1,18,34] With the gas jet, the particle aerosol, formed by the collisional condensation of the ablation plume ablation was effectively transported onto the substrate, positioned at 1.3 cm from the ablation spot. The deposited nanomaterial worked well as a SERS substrate for the chemical detection of Rh6G and crystal violet. The underlying approach provided sufficient room to tune the particle size, surface coverage, and morphological features by working with the laser shot number, substrate distance, gas flow, and laser fluence. Working with the gas flow, the surface redeposition and substrate surface etching by the plasma plume in the case of close proximity deposition was largely eliminated. Furthermore, for the thin films, the deposition process on a remotely spaced substrate was impressively improved.

An ionized gas jet such as formed by the dielectric-barrier discharge (DBD) source can be integrated with the ablation process to enhance the deposition of particle aerosol at atmospheric pressure. Unlike gas flow, the plasma hybrid deposition scheme has great efficacy of transporting material over a longer deposition distance without slowing down significantly. DBD plasma jets are partially ionized gases that operate at energy nonequilibrium, where electrons are at much higher temperature than the atoms and are touchable.^[35–39] In DBDs, excessive and rapid discharge is suppressed by the dielectric (glass, alumina, mica, etc.), resulting in a discharge that does not produce an arc (spark) and for this reason, it is also called a silent discharge. When discharge happens, a charge is accumulated in the dielectric, similar to a capacitor and the discharge occurs at lower voltages when the ac voltage reverses its direction. The jet is characterized by electron number density, $n_e \approx 10^9\text{--}10^{13} \text{ cm}^{-3}$ and temperature, $T_e \approx 1\text{--}10 \text{ eV}$. The DBD streamers propagate at much higher speeds of $10^4\text{--}10^6 \text{ ms}^{-1}$, several orders of magnitude higher than the gas flow and indicate that these plasma jets are driven by the electric fields.^[35,36] Experimental and computational knowledge studies of guided streamers, in particular related to the propagation dynamics of ionization waves, are very useful to materials science and nanotechnology and have been described by various researchers.^[35–39] From a deposition perspective, an interesting feature of the DBD plasma is the electric wind, a spin-off of the plasma electric fields, also known as “ionic or corona wind.” This is a well-known phenomenon and has motivated several studies on the effects of electric fields on fluid flow and mass transfer. Under the upshot of ionic wind, plasma induces a bulk momentum in the gas flow that enhances its speed and subsequently the deposition rate.^[40,41] The use of DBD plasma jets for deposition is an interesting research topic, as it has not been extensively studied in the literature. This method could potentially lead to significant advancements in nanofabrication technology and broaden scientific knowledge across various disciplines.

Here, we describe a hybrid scheme that combines shorter and extended DBD plasma jets with a ns pulsed laser ablation process for the deposition of particulate plasmonic nanostructures of silver. The procedure is based on the mechanism of driving the particle aerosol with a flowing stream of ionized gas jet. The deposition of the nanomaterial with both plasma jets was analyzed and conducted SERS tests to examine the functional nanostructures for chemical detection. Theoretical analysis of the gas flow in the presence of discharge was also done using ANSYS software to support the experimental findings. This scheme addresses pre-existing challenges such as (1) the deposition of wide-range and high-purity materials without using chemical precursors, (2) faster deposition rate and deposition on widely spaced surfaces in an industrially favorable environment, and (3) enabled morphological features and scalable large surface deposition. Encouraging applications include solar cells, catalysis, and sensor.

2. Experimental Section

The experiment involved using an argon plasma jet, produced in the normal and reversed electrode configurations to transport ablation material for deposition on substrates. A quartz, tube reactor was used, with two ring-type metal electrodes,

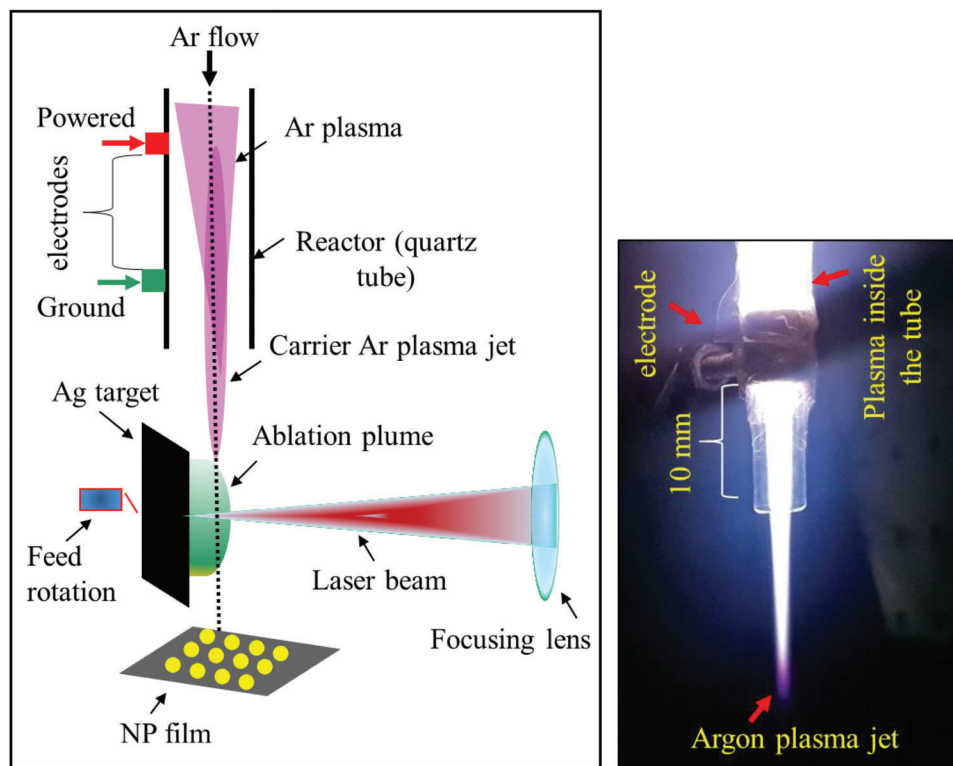


Figure 1. A sketch of the experimental hybrid-plasma APLD setup showing a vertically downstream outflowing plasma jet, focused laser radiation for ablation, plasma plume of silver and nanoparticle deposition on the surface of the substrate. The inset is a photograph of the visible argon plasma jet, penetrating into the ambient air from the downstream open end of the tube.

wrapped around the tube to produce a filamentary-type discharge (Figure 1). The flow rate of argon process gas was controlled by a mass flow controller at the inlet of the quartz tube. An alternating current (ac) of high peak amplitude of $18 - 20 \times 10^3$ V at a frequency of 15×10^3 Hz was applied across the electrodes to excite and sustain the gas discharge. The plasma jet proceeding from the open end of the tube (inset of Figure 1) was adjusted parallel to the target surface as close as possible to enable its interaction with the ablation plume and particle deposition. A 248 nm, 25 ns excimer laser, operating at a repetition rate of 10 Hz was used for ablation. The nanomaterial transported with the plasma jet was collected on glass, silicon, and Cu-TEM grids and examined using electron microscopy, high-resolution transmission electron microscopy (HR-TEM), and absorbance spectroscopy. The discharge properties were examined using a digital oscilloscope, HV probe, and iCCD. SERS measurements of Rhodamine 6G (Rh6G), spread on the substrate were taken using a Raman spectrometer of spectral resolution 2 cm^{-1} , and excitation radiation of 532 nm. An ANSYS software was used to simulate the magnitude of the induced velocity under DBD discharge. The experimental gas discharge condition and deposition parameters are listed in Table 1.

3. Results and Discussion

The electrical and optical measurements of the plasma were performed to understand the mode of operation of the plasma device. The high-voltage ac and current waveforms of the plasma

were measured, and it was observed that the plasma operated in a filamentary regime, with a single large current peak and small current traces appearing per half-cycle of the ac voltage (Figure 2a). The magnitude of the current traces was almost twice in the negative half-cycle, indicating effective discharge during this cycle. Upon electrical excitation, a visible plasma is formed inside the tube, which extended beyond the tube orifice as a long luminescence plasma jet (Figure 2b). The plasma density in the active region was estimated to be around $n_e \approx 10^{13} \text{ cm}^{-3}$. The formation mechanisms of such plasma jets have been explained in the previous literature.^[35–40]

The deposition of NPs by the plasma jet on Si was examined by scanning electron microscope (SEM) at two different magnifications (Figure 3a,b). For the substrate position of 0.8 cm, the length of the plasma jet was sufficient for interaction with the surface. It was observed that the plasma jet resulted in a large deposit of material on the surface compared with no plasma condition and it also facilitated the formation of large-size agglomerates. However, it was unclear whether these agglomerates were formed during the interaction of the plasma jet with the ablation plume or after the deposit had set on the surface. The deposition of nanomaterials under no plasma condition is described in our previous studies.^[1,34] Under no plasma condition when the discharge is off, the particle is flowed in the gas to deliver it to the substrate. It was observed that the film with the plasma was more blackish in appearance, and the strength and spectral features of the surface plasmon resonance (SPR) of the plasma-driven nanostructures were significantly different (Figure 4). The

Table 1. Experimental conditions/parameters of pulsed laser ablation and plasma ignition.

Pulsed laser ablation		Plasma	
Laser-type	Excimer 25 ns	Plasma source	DBD
Pulse duration		Reactor type	Quartz tube
Ablation spot	0.74 cm ²	Excitation voltage	18–20 kV
Laser HV	26 kV	Frequency	15 kHz
Laser fluence	3.4 J·cm ²	Electrode	Ring type (Cu)
Ablation media	Gas flow, plasma	Process gas	Argon
Laser wavelength	248 nm	Gas flowrate	3.5–7.0 lit. min ⁻¹
Rep. rate	10 Hz	Plasma density	6.5 × 10 ¹³ cm ⁻³
Laser power	7 W	Gas feed tube (id/od)	2.4/3.0 mm
Deposition time	600 s	Discharge type	ac filamentary
Deposition distance	8–35 mm	Discharge current	5 mA

broad feature of SPR stretching in the IR region (spanning over the spectral region from 320 to 800 nm) indicated an interactive behavior of the particles due to dipole–dipole interaction, which was increased with an increase in particle size and decreased with an increase in interparticle separation and is approximated by $(R/d)^{2L+1}$ where R and d are the particle size and interparticle separation, respectively, and L is the multipole order with $L = 1$ for the dipole and 2 for the quadrupole. This led to a red-shift in the spectral wavelength of the SPR absorption.^[42–45] The SPR broad features are associated with both intrinsic and extrinsic properties of the film.^[42,43] The discussion leads two conclusions, first, the plasma jet enhances the deposition rate, which can be linked to the phenomenon of electro-hydrodynamic gas pumping (EHD) induced by the presence of high electric fields in the plasma region. Second, the plasma jet promotes particle clustering (agglomerates), which could be due to the presence of charge imbalance on the particles that creates a Coulomb attractive force and holds the particles together.^[46–48] The attachment of electrons to relatively large-size particles makes them negatively charged. The interaction of these particles with the uncharged smaller-size particles generates a stochastic charge fluctuation, which results in a net attractive force between the particles, keeping the particles stuck together physically.^[47] In addition, the dusty plasma framework can be used to explain the interaction of plasma and metal particles as a hybrid system.^[48] Another significant aspect is the plasma turbulence effect, especially in the context of an electro-hydrodynamic (EHD) jet. The fluid instability of the EHD jet induces turbulence onset, which causes the mixing of the argon and the surrounding air. This mixing results in the formation of more than one preferential pathway through which the plasma plume can propagate, leading to the branching of the plasma front.^[49] As a consequence, expectedly, it also leads to collisionality and resulted in particle clustering and the stochastic insurgence of anomalous clusters. Additionally, turbulence promotes air entrainment in the plasma plume, which can result in the oxidation of particles with the formation of reactive oxygen species. This was clearly observed in the EDX results not shown here as well as indicated by the blackish color of the deposit. However, the potential onset of turbulence, typically associated with the propagation of an ionic wind pressure wave along the plasma plume is not considered in the current study due to its limited scope.

However, the literature contains interesting reports on these crucial aspects.^[49,50]

The deposit was further characterized using HIM, TEM, HR-TEM, and the images are displayed in **Figure 5a–c**. The particle size distribution in **Figure 5a** was obtained by making analysis in ImageJ software. Consistent with the SEM study, particle aggregates were also clearly visible in the HIM and TEM micrographs. The images obtained from the characterization techniques helped to better describe the particle morphology and define surface features with more clarity. The fringe formation in the HR-TEM image indicates the crystalline nature of the particle. In the HIM image, apart from agglomerated particulates, the surface also showed isolated particles of mean Feret diameter ≈ 20 (14) nm with the number in the bracket denoting the standard deviation in the particle size. To understand the dependence of the particle deposition on the jet length, a particle film was made with the plasma jet excited in flowing argon at 3.5 lit. min⁻¹. The substrate was moved farther away downstream of the tube orifice to prevent the pronounced interaction of the plasma jet with the surface and avoid surface etching. For 3.5 lit. min⁻¹, the jet length was significantly increased to ≈ 40 mm. The HIM and SEM of the films made on Si under his condition are shown in **Figure 6a,b**, respectively. For this discharge, the plasma jet length is about two times larger than in the previous case and the thickness of the jet varies over the entire length with a considerably thinner morphological feature at the tail. The altered interaction of the needle-like narrow tail with the surface leads to a particle distribution that is different from the previous case. In this case, the substrate shows a sparse distribution of isolated particles with an angle average size of about 11 (5) nm, obtained from the lognormal function, fitted to the particle Feret size distribution histogram. Apart from the population of isolated particles, large features were also observed as indicated by the red circle in image (**Figure 6a**). The formation of such features with the argon plasma jets is the discharge induced effect and is not fully understood at this stage. **Figure 7a,b** shows the deposit obtained with the plasma jet operated in reversed mode by setting the live electrode downstream and ground upstream of the reactor, while the rest of the plasma conditions persist. In this configuration, plasma jet was not emitted in regular fashion; however, plasma bullets were observed outside the reactor in a random manner.

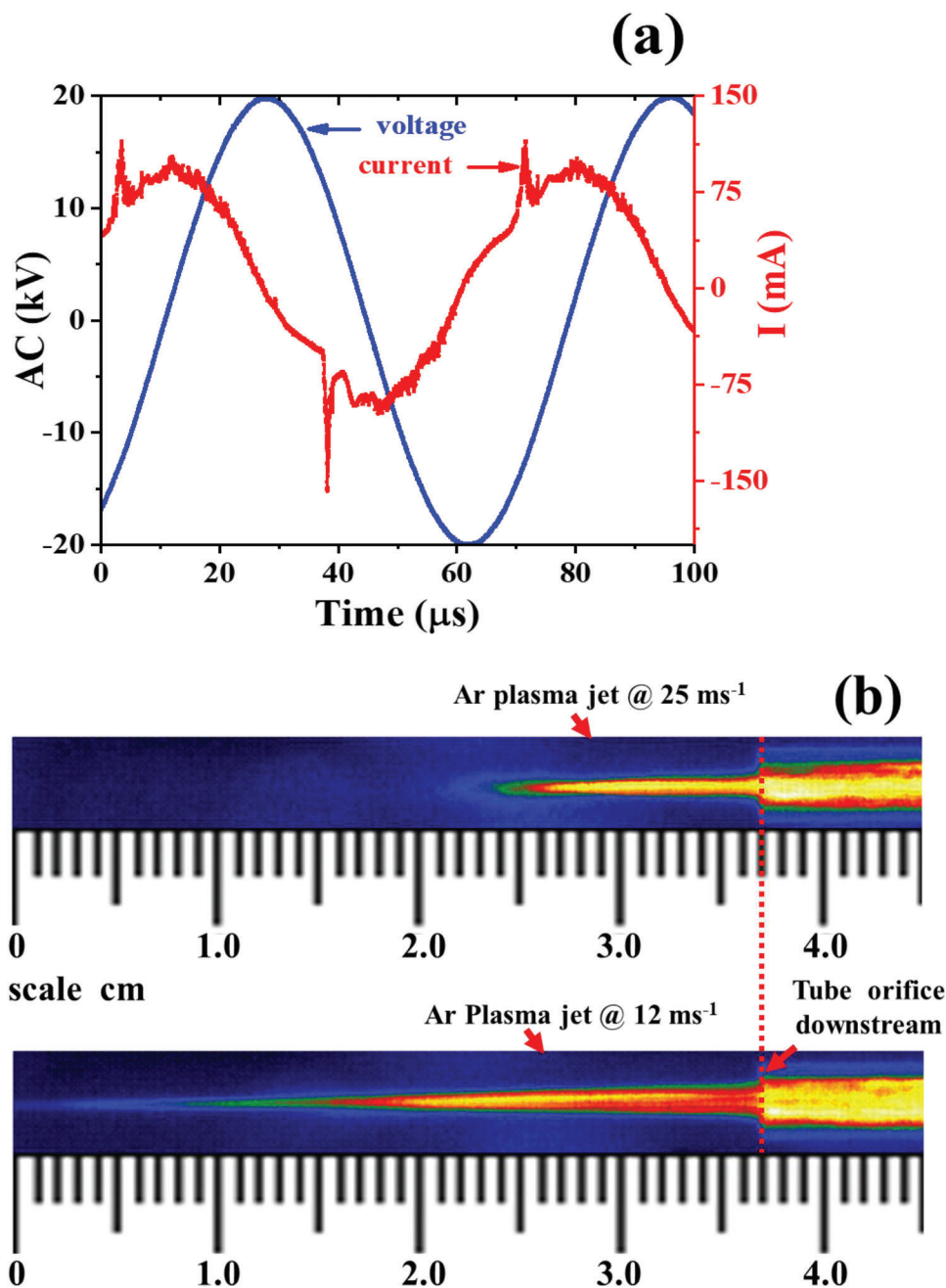


Figure 2. a) The typical waveforms of applied ac voltage and the discharge current of argon DBD plasma. b) The optical images of the plasma jet generated at 7 and 3.5 lit. min⁻¹ in argon flow and recorded with an iCCD camera for 3 ms (reproduced with copyright permission from Springer Nature^[34]). The vertical red dotted line indicates the tube outlet from where the plasma jet emanates in the open ambient.

Again, there was a significant increase in the surface coverage and particles are clustered likely observed in the normal mode operation of the plasma. The surface also showed deposit of interesting features (see inset of Figure 7a). The deposit in these cases was relatively less compared with the normal mode case. This could be possibly attributed to the less EHD effect of the plasma when operated in the reversed mode operation. Nevertheless, this clearly indicates that the large deposit obtained with the plasma is associated with the additional flow velocity induced

by the discharge. The actual magnitude of the induced velocity is not very clear in the two cases and needs further detailed investigation to come up with a better understanding of the effect. For the normal mode, a theoretical description exists and is presented in the last section. We also noticed that in each case the plasma stream does facilitate the formation of particle aggregates. It is noteworthy that the aggregate behavior of silver nanoparticles is of high significance in connection to sensing, antibiotics in marine biology and many more.

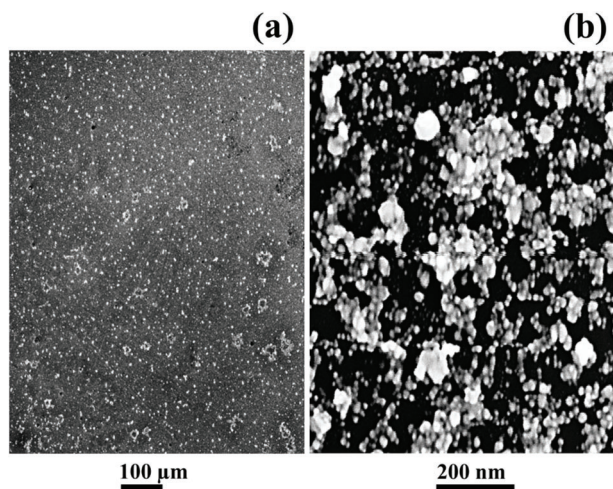


Figure 3. a,b) SEM images of silver particulate film deposited with the plasma jet, excited in argon, flowing through the quartz tube at 7 lit. min⁻¹, on Si, placed at 8 mm from the tube orifice with the downstream orifice of the tube is positioned at 2 mm from the laser ablation spot on the target.

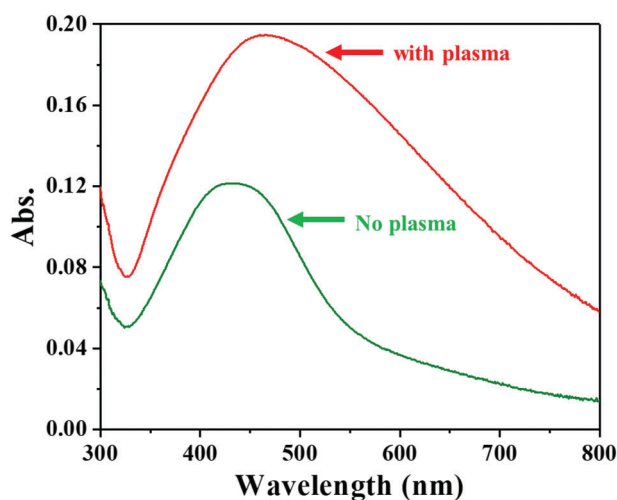


Figure 4. Surface plasmon resonance absorbance of silver nanoparticle films produced with the discharge on (red curve) and off (green curve) on quartz surface, positioned at 8 mm from the outlet of the tube and 6 mm from the ablation spot. For the baseline correction, a reference absorbance of the bare quartz surface was used.

For the distribution of ablation material on the substrate, a scanned image of the deposit obtained with a flatbed scanner was analyzed in Gwydion software. The flatbed-scanned image was recorded with a resolution of 150 dots per inch (dpi) and processed in Gwydion as shown in Figure 8a. This image showed a variation in material distribution, with a thick deposit near the plasma-surface interaction zone and a rarefied region with less deposit toward the peripheral region. Radial surface profiles obtained with a fixed resolution of 100 px over the regions indicated by the arrows are shown in Figure 8c. The line scans indicate the thicker region with more deposits (marked as 1–5), and the outer thinner region with less deposit (marked as 6 and 7). Figure 8d is the curve obtained for the film region, enclosed by the red rectangle in Figure 8a and shows an average film roughness of ≈ 72.22

± 26.27 nm. Additionally, a 1-dimensional fast Fourier transform (1D-FFT) image (Figure 8b obtained in the horizontal direction for the indicated thicker region from the Fourier Modulus Density (FMD) curve), (not displayed here) indicated the formation of a single-phase crystalline nature of the particulate structure. These results demonstrate that the quality and associated SPR characteristics of the film strongly depend on the plasma deposition conditions.

Noble metal nanostructures such as nanosilver possess localized surface plasmon resonances (LSPRs) that give them useful optical properties, particularly for surface-enhanced Raman spectroscopy (SERS).^[4–7,51] A widely accepted mechanism for surface-enhanced processes is predominantly electromagnetic in nature.^[52] The plasma-produced nanosilver-coated surface was tested in SERS for the chemical detection of Rhodamine 6G (Rh6G), and the SERS performance was quantified in terms of Signal-to-Noise Ratio (SNR) and Apparent Enhancement Factor (AEF). The average SERS spectra showed well-defined phonon bands in the spectral region of 300–1800 cm⁻¹ (Figure 9). The results SNR and AEF were calculated using statistical analysis and compared with a commercially available substrate and the silver film previously reported in ref. [1]. Rhodamine 6G (Rh6G) of strength 2.7×10^{-5} M was spread on the coated surface and excited by 532 nm laser radiation, which was focused through a 100× objective lens. The plasma-produced SERS substrate exhibited peaks of Rh6G with more clarity than in previous studies in ref. [1], with an SNR of 2.09×10^2 and an AEF of 9.23×10^2 . Although the plasma-produced SERS substrate had large agglomerates which were not effective for point-to-point reproducible SERS signals, it was still useful for detection purposes in the lab. There are possibilities to reduce and control agglomerate formation to improve its SERS performance. In addition to SERS, the plasma-assisted method studied here is suitable for the deposition of catalytic materials such as Ni, Pt, Pd, and photoactive oxides such as TiO₂ for applications in optical and chemical catalysis.

4. Theoretical Description

An interesting aspect of particle deposition with nonthermal plasma jets is the increased deposition rate. This can be explained in terms of the flow velocity induced by the discharge. To understand this fact, a brief theoretical analysis, based on the conservation laws, was considered without taking into account the viscous effect of the fluid, which deteriorates the operation of the DBD plasma device. For the 1D geometry, the volumetric force F due to the applied electric field E of the applied ac voltage on the gas flow in the main discharge region can be expressed as follows:

$$F = e * \Delta n * E \quad (1)$$

where e is the charge of an electron, and Δn is the plasma charge density (usually the difference between positive and negative charge species).

$$\text{Since } \nabla \cdot E = \frac{e * \Delta n}{\epsilon_0} \quad (2)$$

(Poisson Equation)

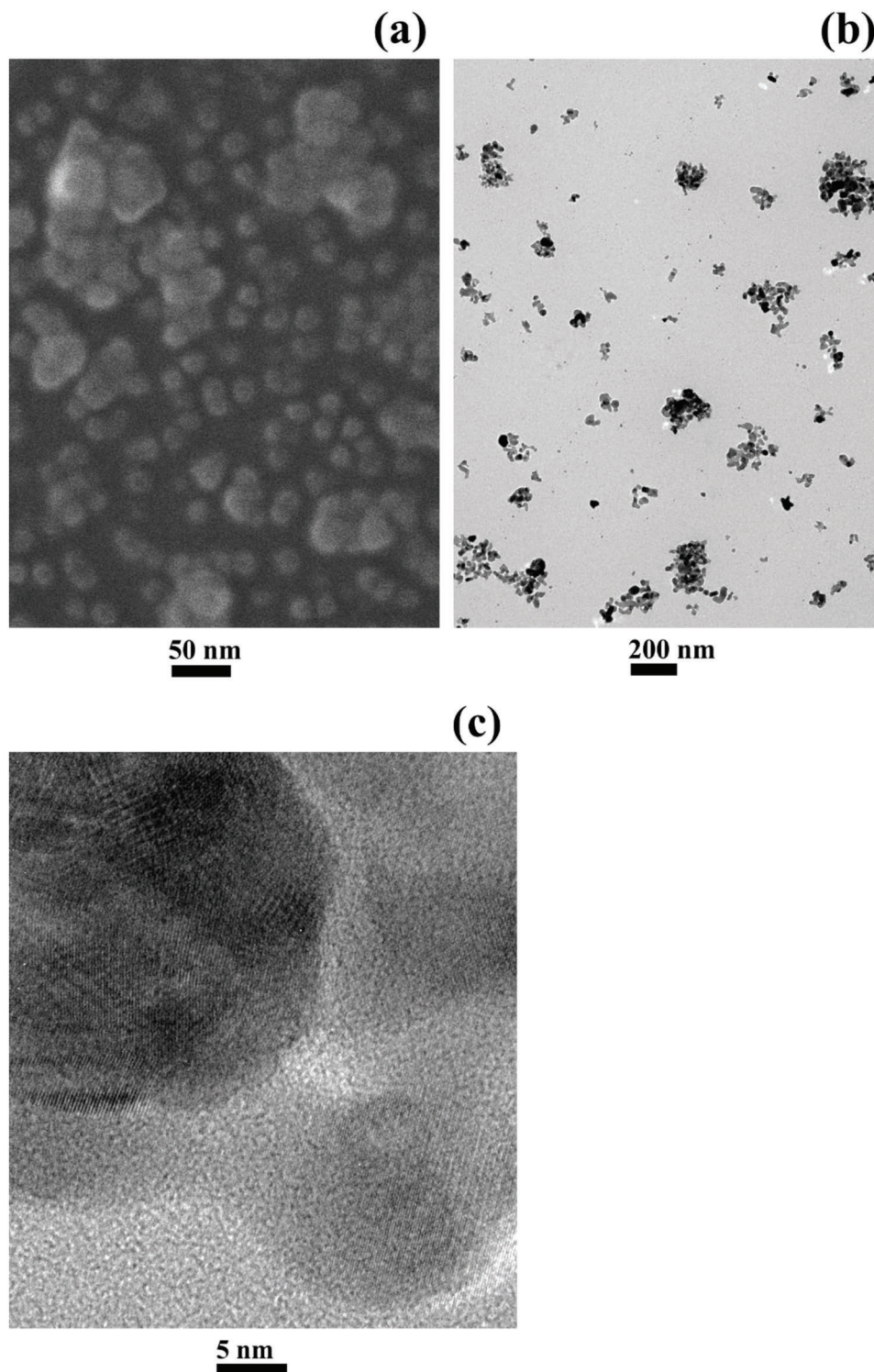


Figure 5. Silver particulate film produced with argon plasma ignited at 7 lit. min^{-1} on Si, Cu-TEM- grids with amorphous carbon film and examined with: a) Helium ion microscopy, b) transmission electron microscopy, and c) high-resolution transmission electron microscopy. The HRTEM image (c) is reproduced with copyright permission from Springer Nature^[34].

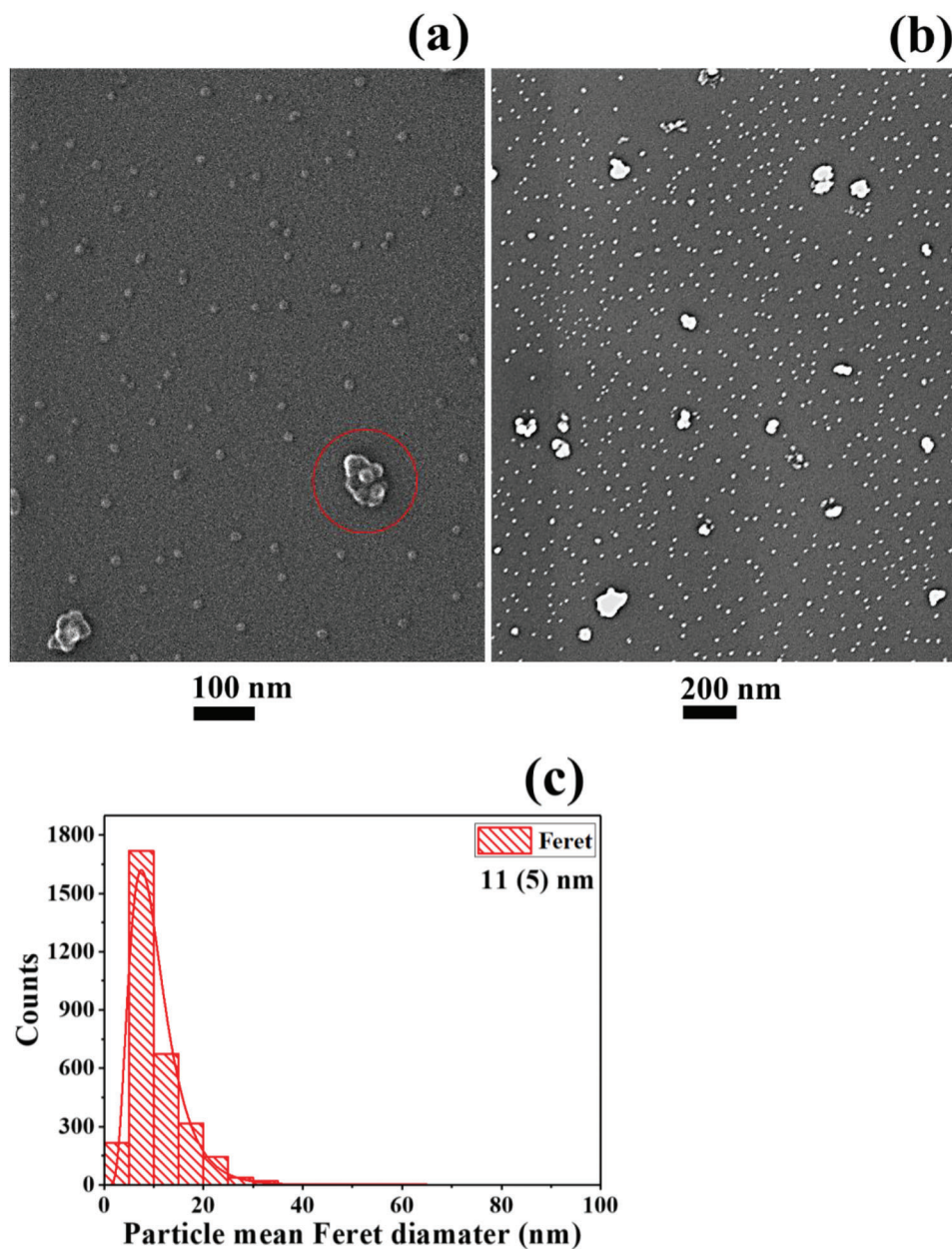


Figure 6. a) Helium ion microscopy and b) SEM images of silver nanoparticle produce by plasma assists hybrid scheme at $3.5 \text{ lit. min}^{-1}$ with the substrate positioned at 35 mm downstream from outlet of the tube. c) The particle Feret diameters distribution obtained for the image in (a). The red circle in (a) indicates the formation of large-clustered structures. (This SEM image is reproduced with copyright permission from Springer Nature^[34]).

where ϵ_0 is the dielectric permittivity of free space with a value of $8.854 \times 10^{-12} \text{ F m}^{-1}$.

By combining Equations (1) and (2), we get the expression for the force in terms of the electric field;

$$F = \frac{1}{2} \epsilon_0 \nabla E^2 \quad (3)$$

Due to this force, the working gas feed in the tube will feel a momentum downstream in the forward direction. Thus, if V_0 is the gas flow velocity upstream the DBD region (without plasma effect) and V is the gas velocity downstream the DBD region (with

plasma effect), then by momentum equation, we have

$$\frac{1}{2} \rho V^2 = \int F \cdot ds + \frac{1}{2} \rho V_0^2 \quad (4)$$

By substituting Equation (3) in Equation (4) and simplifying we get

$$\frac{1}{2} \rho V^2 = \frac{1}{2} \epsilon_0 E^2 + \frac{1}{2} \rho V_0^2 \quad (5)$$

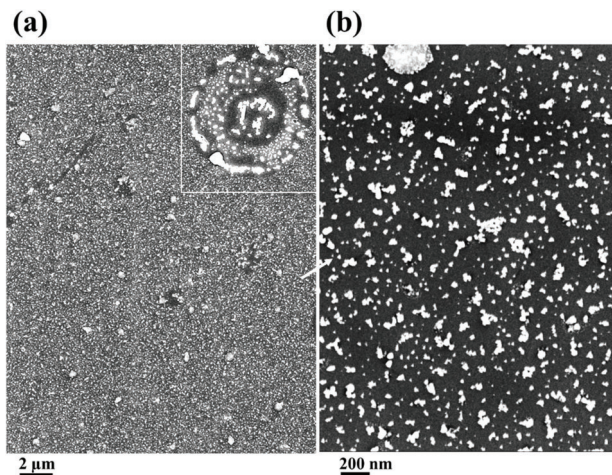


Figure 7. SEM images showing surface nanofeatures of Si, covered with silver nanoparticles using an argon plasma jet, launched in the reversed mode by setting the live electrode downstream and ground upstream of the reactor while the rest of the plasma conditions persist.

where ρ is the density of the gas, which is argon in this case.

$$Eq.5 \Rightarrow V = \left(\frac{\epsilon_0 E^2}{\rho} + V_0^2 \right)^{\frac{1}{2}} \quad (6)$$

Expression in Equation (6) estimates the final velocity of the gas flow with an induced velocity term $\frac{\epsilon_0 E^2}{\rho}$.

The maximum limit of the plasma induced flow velocity in the absence of any flowing gas ($V_0^2 = 0$) is given by:

$$\Rightarrow V = \left(\frac{\epsilon_0 E^2}{\rho} \right)^{\frac{1}{2}} \quad (7)$$

It is notable regarding the modeling of the ionic wind (gas flow), Equation (2) indicates that the electric field arises from the charge imbalance, yet later on, the electric field is calculated from the applied voltage to keep the problem simple. The ANSYS software does not model any electric field effect and just models the flow at a higher flow velocity leaving the tube. Similarly, any increase or decrease in the gas density is neglected if the gas flow is accelerated as it moves between the electrodes. For argon gas of density $\rho = 1.2 \text{ kg m}^{-3}$ and with the maximum electric field in the discharge region of max magnitude $E[V/m] = V_{\text{voltage}}/d$ (where V_{voltage} is the ac voltage across the electrodes and d is the interelectrode separation), the possible maximum numerical value of the DBD induced gas flow velocity V_{max} at atmospheric conditions is about 70 m s^{-1} . Thus, for an argon gas flow velocity of 32 m s^{-1} , the maximum possible theoretical outflow velocity of magnitude 75 m s^{-1} could be obtained with the DBD discharge. This determines the maximum limit of DBD-induced velocity in a gas flow at atmospheric pressure. Instead, these values are much higher than the simulated values obtained by ANSYS, presented in **Figure 10a,b**. The velocity contours displayed in **Figure 10a,b** indicate that in the presence of DBD discharge, the magnitude of the maximum induced velocity achieved was about 31.5 m s^{-1} (@3.5 lit. per min) and 44.5 (@ 7 lit. per min)

m s^{-1} . These values are smaller than the maximum values described by Equation (7). The experimental values could be even further smaller because up till now, to the best of our knowledge, nobody has reported such a large increase in the induced velocity by the DBD discharge. However, this result makes one thing quite obvious: the plasma imparts some momentum to the bulk flow of the gas due to the electric fields that exist in the discharge regime and speeds up the gas flow as described by Equation (7). Consequently, the faster gas flow in the presence of the discharge carries the nanomaterial more effectively at atmospheric pressure to the substrate and leads to an enhanced deposition rate. Furthermore, due to the electrical nature of the plasma jet, it is difficult to obtain accurate flow velocity measurements using traditional Pitot tubes, as an electrical breakdown occurs at the interface of the plasma jet and the flow detection probe. To further understand the effect of the plasma-induced gas flow velocity on deposition rate, it is suggested that a dielectric Pitot tube could be used to measure the actual value of the plasma-induced gas flow velocity in the presence of DBD plasma.

5. Conclusion

In summary, the paper explored a hybrid plasma-assist scheme of deposition that combines the benefits of both DBD plasma jet and ns pulsed laser ablation. By using ionized gas to drive the particle aerosol, the deposition of high-purity materials without the use of chemical precursors was made possible at ambient conditions. Additionally, the faster deposition rate and the ability to deposit particles on widely spaced surfaces with altered morphologies make this scheme industrially favorable. The surface nanofeatures strongly depend on the jet interaction with the substrate, substrate position, and jet length. For substrate at the extended position, particles exhibited sparse distribution, while close to the ablation zone, these were assembled in large aggregates. In the reverse mode operation, the particle deposition was less than in the normal operation but with similar morphological features. While the substrate was found better for SERS, the signals were not reproducible due to the large spatial variation of the particle nanofeatures as well as surface coverage. The theoretical simulation showed that the gas flow velocity was increased with the discharge, leading to an enhanced deposition rate. The study concludes that the plasma-jet scheme provides a rapid platform to address some of the existing challenges in nanofabrication and suggests an interesting extension of the scheme to multicomponent hard plasmonic nanostructures of titanium nitride (TiN) for applications in antimicrobial, microelectronic, and surgical devices. There is a need to consider the potential onset of turbulence, associated with the propagation of an ionic wind pressure wave along the plasma plume to explain the increased clustering and the oxidation of nanoparticles.

Declarations

On behalf of all the coauthors, I take full responsibility for this submission. All the authors listed on the title page have contributed knowingly, have read the manuscript, attest to the validity and correctness of the data and its interpretation, and agree to the submission.

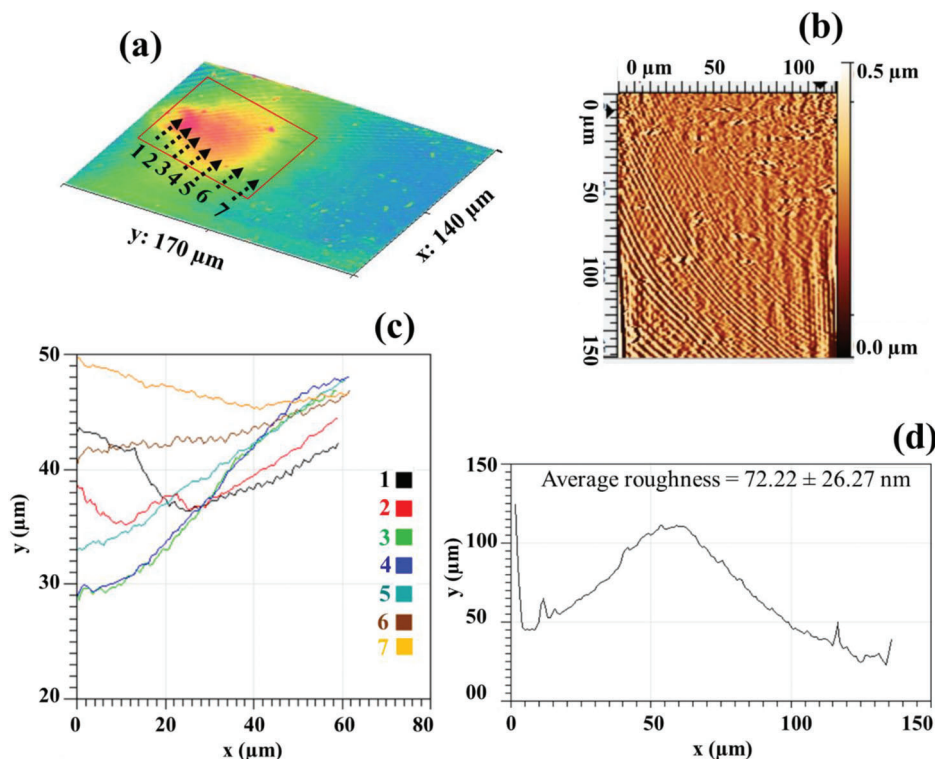


Figure 8. a) Calibrated flatbed scanner image of silver deposit recorded with a resolution of 150 dots per inch (dpi); b) 1-D FFT image for the indicated region in (a); c) the surface radial profiles for the indicated regions 1–7; and d) average roughness obtained for the whole film region shown in (a).

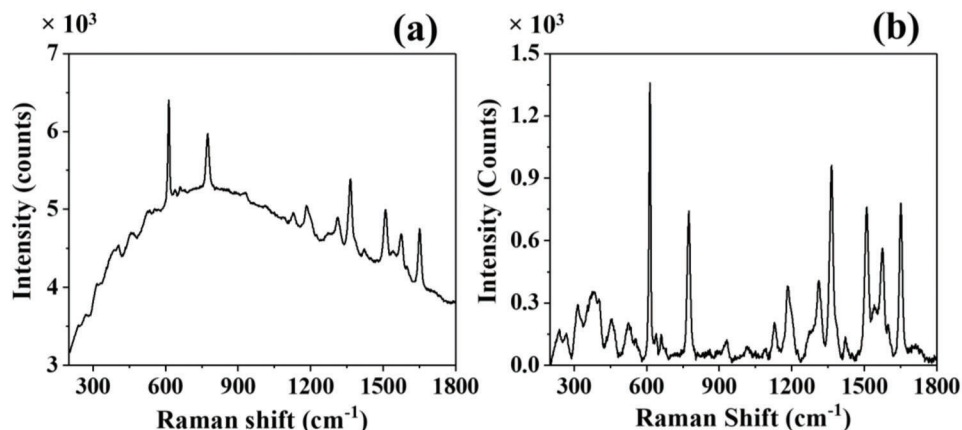


Figure 9. SERS spectra of Rh6G dye (2.7×10^{-5} M) measured on plasma-produced silver films: a) with background and b) without background, using laser excitation wavelength 532 nm and exposure time 5 s (with copyright permission from Springer Nature).^[18] The calibration of the system was done with a silicon surface using the peak at 521.237 cm^{-1} and for background correction, a polynomial of degree 8 was used.

Ethics Approval and Consent to Participate

All the coauthors give their ethical approval and consent for the publication of identifiable details enclosed in the manuscript.

Consent for Publication

All the coauthors have given their consent and agreed to the publication of the work.

Acknowledgements

This research was initiated and directed by Dr. James G Lunney. This research was supported by a grant from the Science Foundation Ireland (SFI) under Investigator Project 12/IP/1662, where Dr. James G Lunney was the principal investigator, and national funds through FCT– Fundação para a Ciência e a Tecnologia, under the project UIDB/00285/2020, and LA/P/0112/2020. The funding sources have been declared.

Conflict of Interest

The authors declare no conflict of interest.

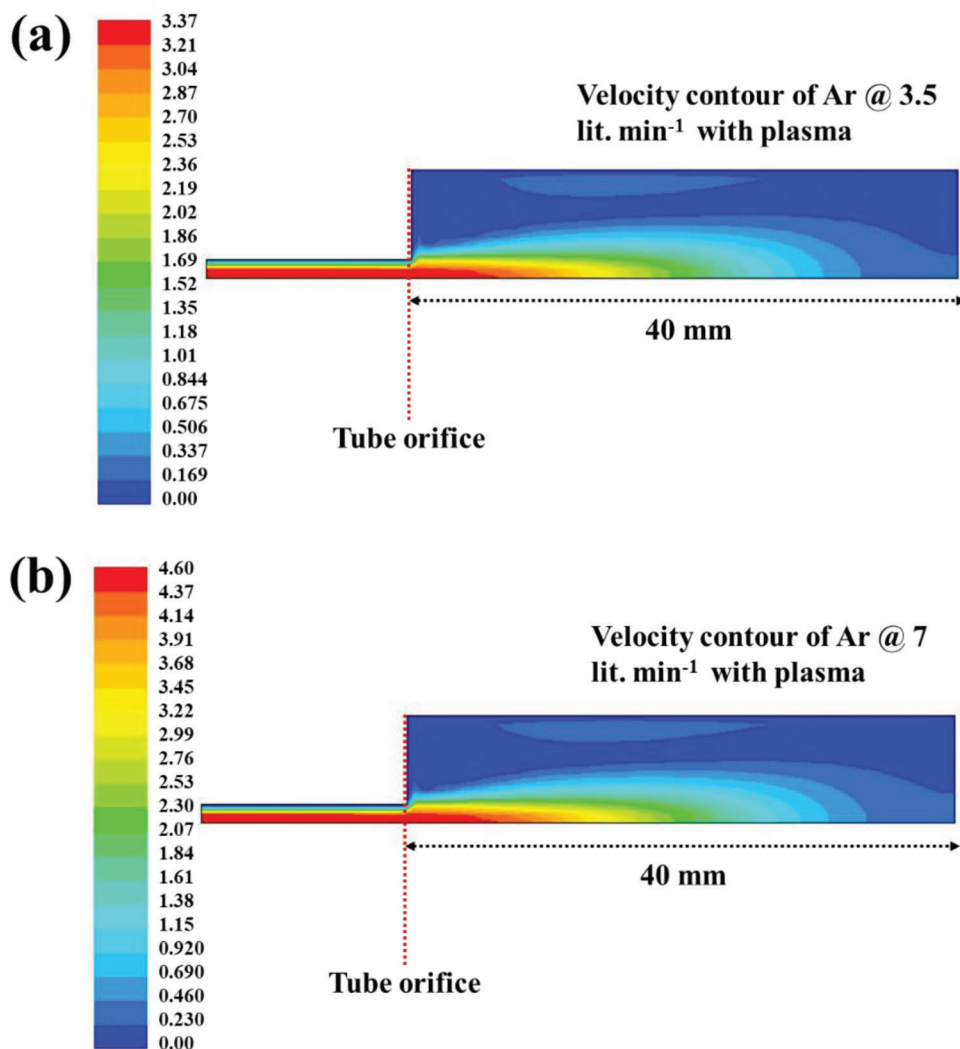


Figure 10. Velocity magnitude contours: a) and b) [$\times 10^1$], of argon flow theoretically simulated at 3.5 and 7 lit. min⁻¹ with the DBD plasma operated in the tabular geometry and electrodes separation of 20 mm. The red dotted line indicates exit of the tube from where the plasma outflow emanates into the ambient air.

Data Availability Statement

The data that support the findings of this study are available from the corresponding author upon reasonable request.

Keywords

argon plasma jet, computational analysis, helium ion microscopy, high-resolution transmission electron microscopy, plasmonic surfaces

Received: April 8, 2023

Revised: May 7, 2023

Published online: June 30, 2023

[1] T. M. Khan, M. A. Mujawar, K. E. Siewerska, A. Pokle, T. Donnelly, N. McEvoy, G. S. Duesberg, J. G. Lunney, *Nanotechnology* **2017**, *28*, 445601.

- [2] C. Wei, M. Li, X. Zhao, *Front. Microbiol.* **2018**, *9*, 2857.
- [3] T. V. Pfeiffer, J. Ortiz-Gonzalez, R. Santbergen, H. Tana, A. SchmidtOtt, M. Zeman, A. H. M. Smets, *Energy Procedia*. **2014**, *60*, 3.
- [4] Y. Sun, *Nanoscale* **2010**, *2*, 1626.
- [5] J. Linnet, A. R. Walther, C. Wolff, O. Albrektsen, N. A. Mortensen, J. K. Hansen, *Opt. Mater. Express* **2018**, *8*, 1733.
- [6] S. Shen, S. Chen, D. Zhang, Y. H. Liu, *Opt. Express* **2018**, *26*, 27545.
- [7] C. H. Liu, X. Yu, *Nanoscale Res. Lett.* **2011**, *8*, 75.
- [8] C. Zhang, N. Kinsey, L. Chen, C. Ji, M. Xu, M. Ferrera, X. Pan, V. M. Shalaev, A. Boltasseva, L. J. Guo, *Adv. Mater.* **2017**, *29*, 1605177.
- [9] X.-F. Zhang, Z.-G. Liu, W. Shen, S. Gurunathan, *Int. J. Mol. Sci.* **2016**, *15*, 1534.
- [10] S. H. Lee, B.-H. Jun, *Int. J. Mol. Sci.* **2019**, *20*, 865.
- [11] M. A. Barkat, B. S. Harshita, M. J. Naim, F. H. Pottoo, S. P. Singh, F. J. Ahmad, *Recent Pat. Antiinfect. Drug Discov.* **2018**, *13*, 53.
- [12] J. V. Baudrit, S. M. Gamboa, E. R. Rojas, V. V. Martinez, *Int. J. Biosen. Bioelectron.* **2019**, *5*, 166.
- [13] A. V. Filip, B. A. Sava, R. V. Medianu, L. Boroica, M. C. Dinca, R. Pascu, N. Tigau, A. Andrei, A. Moldovan, M. Dumitru, M. Oane, M. Eftimie, *Inorganics* **2022**, *10*, 235.

- [14] M. Mäkelä, T. Hatanpää, K. Mizohata, K. Meinander, J. Niinistö, J. Räisänen, M. Ritala, M. Leskelä, *Chem. Mater.* **2017**, *29*, 2040.
- [15] R. Eason, *Pulsed Laser Deposition of Thin Films: Applications-led Growth of Functional Materials*, 1st ed., Wiley, New York, **2007**. <https://doi.org/10.1002/0470052120>
- [16] C. A. Smyth, I. Mirza, J. G. Lunney, E. M. McCabe, *Appl. Surf. Sci.* **2013**, *264*, 31.
- [17] I. Mirza, G. O'Connell, J. J. Wang, J. G. Lunney, *Nanotechnology* **2014**, *25*, 265301.
- [18] T. M. Khan, J. G. Lunney, D. O'Rourke, M. C. Meyer, J. R. Creel, K. E. Siewierska, *Appl. Phys. A* **2019**, *125*, 659.
- [19] T. E. Itina, J. Hermann, A. Voloshko, M. E. Povarnitsyn, V. Fokin, P. Levashov, K. V. Khishchenko, A. V. Kabashin, P. Delaporte, presented at *Nanoparticle Formation by Laser Ablation in Gases, Liquids: Modelling, Computational Approaches, 12th International Conference on Laser Ablation, COLA 2013, Book of Abstracts*, Ischia, Italy, October **2013**. pp. 59. <https://www.hal.inserm.fr/OPENAIRE/ujm-00878671>
- [20] H. Jadhav, A. K. Singh, S. Sinha, *Mater. Chem. Phys.* **2015**, *162*, 279.
- [21] R. McCann, C. Hughes, K. Bagga, A. Stalcup, M. Vázquez, D. Brabazon, *J. Phys. D: Appl. Phys.* **2017**, *50*, 245303.
- [22] T. Donnelly, J. G. Lunney, *Appl. Surf. Sci.* **2013**, *282*, 133.
- [23] J. Thomas, H. C. Joshi, A. Kumar, R. Philip, *Phys. Plasmas* **2018**, *25*, 103108.
- [24] V. I. Konov, T. V. Kononenko, E. N. Loubnin, F. Dausinger, D. Breiting, *Appl. Phys. A* **2004**, *79*, 931.
- [25] T. V. Kononenko, V. I. Konov, E. N. Loubnin, F. Dausinger, *Quantum Elec.* **2003**, *33*, 189.
- [26] Z. Ouyang, L. Meng, P. Raman, T. S. Cho, D. N. Ruzic, *J. Phys. D: Appl. Phys.* **2011**, *44*, 265202.
- [27] H. P. Wang, J. Lin, *Surf. Coat. Technol.* **2010**, *204*, 2246.
- [28] N. Nedyalkov, A. Nikolov, P. Atanasov, M. Alexandrov, M. Terakawa, H. Shimizu, *Opt. Laser Technol.* **2014**, *64*, 41.
- [29] M. Boutinguiza, R. Comesaña, F. Lusquiños, A. Riveiro, J. D. Vel, J. Pou, *Appl. Surf. Sci.* **2015**, *336*, 108.
- [30] H. Jadhav, A. K. Sing, S. Sinha, *Mater. Chem. Phys.* **2015**, *162*, 279.
- [31] B. Gao, S. Zhang, X. Ju, Y. Lin, X. Wang, *AIP Adv.* **2017**, *7*, 095206.
- [32] R. G. Nikov, A. O. Dikovska, N. N. Nedyalkov, G. V. Avdeev, P. A. Atanasov, *Beilstein J. Nanotechnol.* **2017**, *8*, 2438.
- [33] A. Białous, M. Gazda, K. Grochowska, P. Atanasov, A. Dikovska, N. Nedyalkov, J. Reszczyńska, A. Zaleska-Medynska, G. Śliwiński, *Thin Solid Films* **2016**, *601*, 41.
- [34] Taj M. Khan, A. Pokle, J. G. Lunney, *Appl. Phys. A* **2018**, *124*, 336.
- [35] S. Wu, Z. Wang, Q. Huang, X. Tan, X. Lu, K. Ostrikov, *Phys. Plasmas* **2013**, *20*, 023503.
- [36] X. Lu, Q. Xiong, Z. Jiang, Z. Tang, J. Hu, Z. Xiong, X. Hu, Y. Pan, *Plasma. Sci.* **2008**, *36*, 988.
- [37] N. Jiang, A. Ji, Z. Cao, arXiv:0811.0130 *Phys. Plasmas-Ph.* **2008**. <https://doi.org/10.48550/arXiv.0811.0130>.
- [38] X. Lu, G. V. Naidis, M. Laroussi, K. Ostrikov, *Phys. Rep.* **2014**, *540*, 123.
- [39] J. S. Yagoobi, J. E. Bryan, *Adv. Heat Transf.* **1999**, *33*, 95.
- [40] N. Benard, N. Balcon, presented at *39th Plasmadynamics, Lasers Conference*, Seattle, Washington, USA, 23–26 June **2008**, <https://doi.org/10.2514/6.2008-3792>
- [41] M. Forte, J. Jolibois, J. Pons, E. Moreau, G. Touchard, M. Cazalens, *Exp. Fluids* **2007**, *43*, 917.
- [42] Z. Liu, H. Wang, H. Li, X. Wang, *Appl. Phys. Lett.* **1998**, *72*, 1823.
- [43] K. Takagi, S. Nair, R. Watanabe, K. Seto, T. Kobayashi, E. Tokunaga, *J. Phys. Soc. Jap.* **2017**, *86*, 124721.
- [44] S. Toroghi, P. G. Kik, presented at *Proc. SPIE 8054, Enabling Photonics Technologies for Defence, Security, Aerospace Applications VII, (2011)*, 80540E <https://doi.org/10.1117/12.884045>.
- [45] A. Demchuk, I. Bolesta, O. Kushnir, I. Kolych, *Nanoscale Res. Lett.* **2017**, *12*, 273.
- [46] P. K. Shukla, B. Eliasson, *Rev. Mod. Phys.* **2009**, *81*, 25.
- [47] K. S. Kim, D. J. Kim, J. H. Yoon, Y. J. Park, Y. Watanabe, M. Shiratani, *J. Colloid Interface Sci.* **2003**, *257*, 195.
- [48] T. M. Khan, G. A. S. Alves, A. Iqbal, *Sci. Rep.* **2023**, *13*, 77.
- [49] M. Boselli, V. Colombo, M. Gherardi, R. Laurita, A. Liguori, P. Sanibondi, E. Simoncelli, Augusto Stancampiano, *IEEE Trans. Plasma Sci.* **2015**, *43*, 713.
- [50] M. Boselli, V. Colombo, E. Ghedini, M. Gherardi, R. Laurita, A. Liguori, P. Sanibondi, A. Stancampiano, *Plasma Chem. Plasma Process.* **2014**, *34*, 853.
- [51] J. Kong, K. Qiao, L. Matthews, T. W. Hyde, *Phys. Rev. E* **2014**, *90*, 013107.
- [52] A. Karabchevsky, C. Khare, B. Rauschenbach, I. Abdulhalim, *J. Nanophotonics* **2012**, *6*, 061508.